

South-polar features on Venus similar to those near the north pole

G. Piccioni¹, P. Drossart⁴, A. Sanchez-Lavega⁵, R. Hueso⁵, F. W. Taylor⁶, C. F. Wilson⁶, D. Grassi⁴, L. Zasova⁷, M. Moriconi², A. Adriani³, S. Lebonnois⁸, A. Coradini³, B. Bézard⁴, F. Angrilli⁹, G. Arnold¹⁰, K. H. Baines¹¹, G. Bellucci³, J. Benkhoff¹⁰, J. P. Bibring¹², A. Blanco¹³, M. I. Blecka¹⁴, R. W. Carlson¹¹, A. Di Lellis¹⁵, T. Encrenaz⁴, S. Erard⁴, S. Fonti¹³, V. Formisano³, T. Fouchet⁴, R. Garcia¹⁶, R. Haus¹⁰, J. Helbert¹⁰, N. I. Ignatiev⁷, P. G. J. Irwin⁶, Y. Langevin¹², M. A. Lopez-Valverde¹⁷, D. Luz^{4,19}, L. Marinangeli¹⁸, V. Orofino¹³, A. V. Rodin⁷, M. C. Roos-Serote¹⁹, B. Saggin²⁰, D. M. Stam²¹, D. Titov²², G. Visconti²³, M. Zambelli¹ & the VIRTIS-Venus Express Technical Team*

Venus has no seasons, slow rotation and a very massive atmosphere, which is mainly carbon dioxide with clouds primarily of sulphuric acid droplets. Infrared observations by previous missions to Venus revealed a bright 'dipole' feature surrounded by a cold 'collar' at its north pole^{1–4}. The polar dipole is a 'double-eye' feature at the centre of a vast vortex that rotates around the pole, and is possibly associated with rapid downwelling. The polar cold collar is a wide, shallow river of cold air that circulates around the polar vortex. One outstanding question has been whether the global circulation was symmetric, such that a dipole feature existed at the south pole. Here we report observations of Venus' south-polar region, where we have seen clouds with morphology much like those around the north pole, but rotating somewhat faster than the northern dipole. The vortex may extend down to the lower cloud layers that lie at about 50 km height and perhaps deeper. The spectroscopic properties of the clouds around the south pole are compatible with a sulphuric acid composition.

We used the Visible and Infrared Thermal Imaging Spectrometer (VIRTIS) instrument^{5,6} on the Venus Express spacecraft to observe the south polar region of Venus. VIRTIS measures radiation intensity at wavelengths between 0.3 and 5 μm . The wavelengths between 3 and 5 μm are sensitive to both temperature and cloud opacity variations. Despite the uncertainties that this introduces, extensive radiative transfer modelling indicates that the real temperature profile in the mesosphere (60–100 km altitude) can be retrieved from VIRTIS data with errors of a few kelvin.

The observations in Fig. 1 show that the atmospheric structure at the south pole as seen in the thermal region of the spectrum at about 5 μm exhibits an inverse 'S' shape, indicating a polar dipole having two centres of rotation in an anticlockwise direction (in agreement with the direction of the atmospheric superrotation), surrounded by a cold collar very much like that observed in the north from past

missions. Both the dipole and the collar are thus similar to those previously observed at the north pole by Pioneer Venus⁴ but in mirror image (owing to the clockwise rotation of the atmosphere at the north pole). The horizontal gradient of temperature is greatest at an altitude of about 60 km (the lowest layer effectively probed in the thermal region at about 5 μm), with a brightness temperature as high as 250 K observed inside the dipole in contrast with a temperature as low as 210 K observed in the cold collar region. This is shown in Fig. 2, where the real retrieved temperatures are also reported. The detailed, double-eye structure seen in Figs 1 and 2 is not always observed; an oval-shaped dipole with less contrast and variable morphology is more frequently observed in the VIRTIS data from the first few months of Venus Express operations.

Images of the dipole taken during the first 45 days of the spacecraft at Venus indicate that it rotates with a period of -2.48 ± 0.05 days. The negative sign indicates that the dipole rotates in the direction of the solid body of the planet and the superrotating atmosphere, which is retrograde with respect to the rotation of the Earth and most other planets in the Solar System. This rotation is somewhat faster than the rotation of the northern dipole observed from Pioneer Venus in 1979, which exhibited a rotation period varying from -2.79 days to -3.21 days over the 72 days of observation⁷. It could be that the difference is in part due to hemispherical asymmetry, but temporal variability also seems to have an important role. The variability may be caused by external sources—for example, solar influences—or may be indicative of dynamical instability in the atmospheric circulation. The VIRTIS observations reported here were taken sporadically during spacecraft commissioning, so we cannot yet quantify the variability of the dipole rotation rate. However, further observations will help clarify this question.

The analysis of three-dimensional atmospheric thermal fields retrieved from the measured radiances indicates that regions of cold

¹INAF-IASF (Istituto di Astrofisica Spaziale e Fisica Cosmica), ²CNR-ISAC (Istituto di Scienze dell'Atmosfera e del Clima), ³INAF-IFI (Istituto di Fisica dello Spazio Interplanetario), via del fosso del Cavaliere 100, 00133 Rome, Italy. ⁴LESIA, Observatoire de Paris, CNRS, UPMC, Université Paris-Diderot, 5 place Jules Janssen, 92195 Meudon, France. ⁵Departamento de Física Aplicada I, Escuela Superior de Ingenieros Universidad del País Vasco Alda, Urquijo s/n 48013, Bilbao, Spain. ⁶Atmospheric, Oceanic and Planetary Physics, Department of Physics, University of Oxford, Clarendon Laboratory, Parks Road, Oxford OX1 3PU, UK. ⁷Space Research Institute of Russian Academy of Sciences (IKI), Profsojuznaja 84/32, 117997 Moscow, Russia. ⁸Laboratoire de Meteorologie Dynamique, Jussieu, Box 99, 75252 Paris cedex 05, France. ⁹CISAS Università di Padova, via Venezia 1, 35131 Padova, Italy. ¹⁰German Aerospace Center (DLR), Institute of Planetary Exploration, Planetary Physics Section, Berlin-Adlershof Rutherfordstrasse 2, 12489 Berlin, Germany. ¹¹Jet Propulsion Laboratory, MS 183-601, Pasadena, California 91011, USA. ¹²Institut d'Astrophysique Spatiale, Bâtiment 120, Université Paris-Sud, 91405 Orsay Cedex, France. ¹³Università degli Studi di Lecce, Dipartimento di Fisica, Via Arnesano, 73100 Lecce, Italy. ¹⁴Space Research Centre of Polish Academy of Science, Bartycka 18A, 00-716 Warszawa, Poland. ¹⁵AMDLSPACE s.r.l., Via Giovanni Angelini 33, 00149 Rome, Italy. ¹⁶Département des Études Spatiales, Institut de Physique du Globe de Paris 4, Avenue de Neptune, F-94107 Saint Maur des Fossés cedex, France. ¹⁷Instituto de Astrofísica de Andalucía (CSIC), Camino Bajo de Huétor, 24 Apartado 3004, 18080 Granada, Spain. ¹⁸International Research School of Planetary Sciences, Dipartimento di Scienze, Università d'Annunzio, Viale Pindaro 42, 65127 Pescara, Italy. ¹⁹Observatorio Astronómico de Lisboa, Centro de Astronomia e Astrofísica da Universidade de Lisboa, Tapada da Ajuda 1349-018, Lisboa, Portugal. ²⁰Politecnico di Milano, Polo di Lecco, Via Marco D'Oggiono 18/A, 23900 Lecco, Italy. ²¹Astronomical Institute "Anton Pannekoek", University of Amsterdam, Kruislaan 403, 1098 SJ, Amsterdam, The Netherlands. ²²Max Planck Institute for Aeronomy, Max Planck Str. 2, 37191 Katlenburg-Lindau, Germany. ²³Dipartimento di Fisica, Università de L'Aquila, via Vetoio Loc. Coppito, 67010 Coppito, L'Aquila, Italy.

*A list of participants and affiliations of the VIRTIS-Venus Express Technical Team appears at the end of the paper.

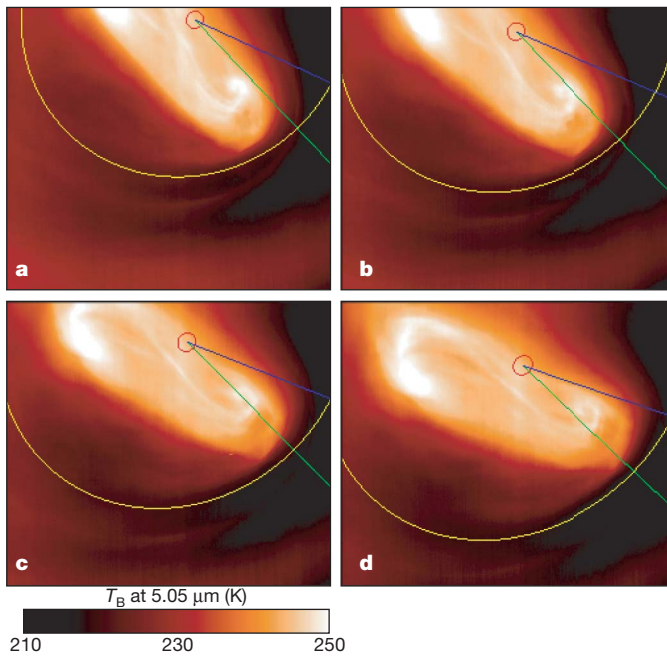


Figure 1 | The Venus south-polar dipole. **a–d**, A sequence of four false-colour images at a wavelength of $5.05\ \mu\text{m}$ acquired during orbit 38 on 28 May 2006, time 17:41:30, starting from **a** with a time interval of 1 hour; the brightness temperature, T_B , is colour coded as shown. The dipole was clearly seen in these observations with unprecedented detail from a distance of about 60,000 km as it rotates around the pole. The images provided by VIRTIS, when used in high spatial resolution mode such as in this figure, have a size of 256×256 pixels and each pixel has an instantaneous field of view of $250\ \mu\text{rad}$. Major and minor axis dimensions of the dipole are about 2,700 km and 900 km, respectively. Radiative transfer calculation sets the main source of the radiance at this wavelength as coming from a layer at about 60 km altitude where the maximum contrast is seen for the detailed thermal structure of the dipole. The blue and green curves in the four panels are the meridians at 330° and 350° of longitude, respectively. The red circle indicates the south pole. The yellow curve is the parallel at -70° of latitude. The cold collar is just beyond this latitude and its temperature is coldest on the right side, where the morning terminator resides. The centre of the dipole in temperature is offset by 4° with respect to the south pole in this image. However we expect some variability, which can be studied over a long term period during the course of the mission.

atmosphere (210 K) are associated with the cold collar at the 100 mbar level (about 65 km altitude). This spatial structure vanishes at higher altitudes (>75 km), where the layers become more spatially isothermal.

Atmospheric vertical temperature gradients between 100 to 50 mbar (about 68 km altitude) appear moderate inside the ‘S’ shape, in the range 0 to $-3\ \text{K km}^{-1}$, whereas strong inversions are observed above the cold collar with values up to $6\ \text{K km}^{-1}$. Another weak

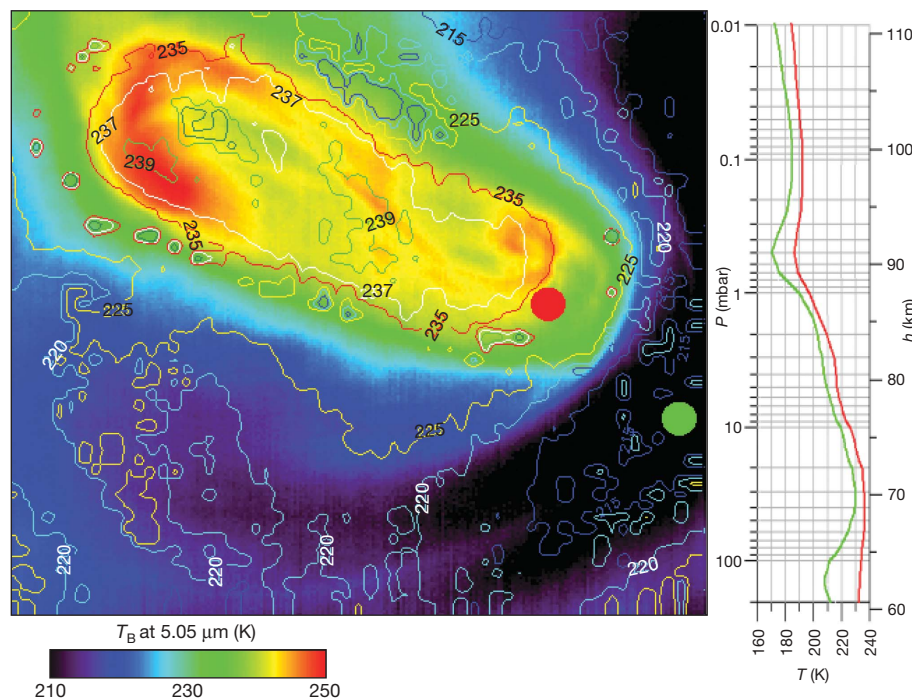


Figure 2 | The dipole in its highest-thermal-contrast atmospheric layer. Left, the colour-coded brightness temperature, T_B , at $5.05\ \mu\text{m}$ of the dipole and the cold collar region. The level curves in the image are the real atmospheric temperatures retrieved from the VIRTIS measured radiances corresponding to a pressure of 200 mbar (about 60 km) and they correlate quite well with the T_B values at this wavelength. The contrast in T_B is maximum at this layer, and the warmer region corresponds to the ellipse containing the dipole where a value of T_B as high as 250 K is observed in the centre of rotation on the left side (real retrieved atmospheric temperature being only a few kelvin less). This part was on the dayside at this time and thus it may be warmed by the solar flux. The overall contrast inside the ellipse is not more than 8 K at $5.05\ \mu\text{m}$. The spatial thermal gradient is steepest from the cold collar to the inner part on the right side of the

right-hand pole of the dipole where a temperature difference of 15 K is observed over a distance of the order of 200 km, just outside the edge of the ellipse. The coldest region of the polar collar with temperatures of about 210 K is registered on the right part, on the morning terminator side. Right, the atmospheric vertical temperature profile in two different regions. The green curve is retrieved in the green spot on the left image, inside the polar collar region. This is also the region where the more prominent thermal inversion is observed in the range from 60 to 70 km altitude. The red curve is from the red spot inside the dipole where the thermal inversion is much more limited. The image also reveals filaments in the circular shape following the rotation of the dipole in the outer part of the ellipse, and also a fine detailed structure in the inner part where the two bright features seem to be connected together.

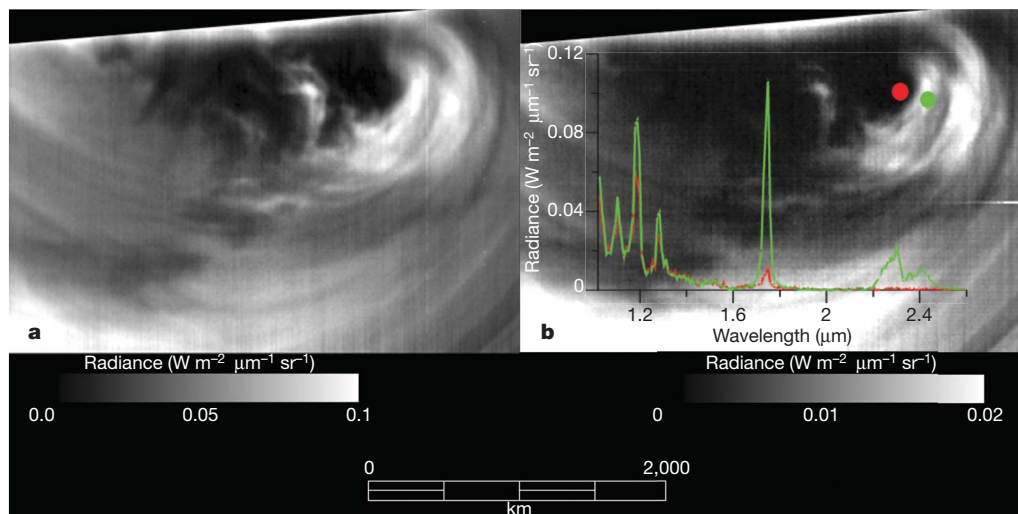


Figure 3 | The deepest view of the dipole seen so far. a, b, Nightside images at 1.74 μm (**a**) and 2.3 μm (**b**) selected from spectral image cube number 4 of orbit 38; radiance is coded according to the grey scale shown. The thermal radiation at these wavelengths mainly originates below the cloud layers, so the structure is produced by spatial variations in the opacity of the clouds. The morphology of the vortex here is remarkable and presents many details. The circular features falling in the region of the cold collar are probably due to clouds elongated by the strong winds coming from the superrotation. The same cloud structures are seen in both spectral regions, with differences in the contrast of the features. The reason for the lower signal at 2.3 μm can be attributed to the different number density or size of the cloud particles^{17,18}. The single scattering albedo for sulphuric acid mode 2 particles is $\omega_0 = 0.99978$ and 0.988 , respectively, for these spectral windows. At 1.74 μm wavelength the signal decreases and at 2.3 μm it becomes dramatically low, sometimes disappearing altogether when the cloud optical depth increases. This is shown in two spectra in **b** related to two different regions, bright

maximum in vertical atmospheric temperature profiles is observed around 0.2 mbar (about 95 km altitude), with a peak temperature ranging from 185 to 195 K and apparently no clear spatial organization. The coldest side of the cold collar is identified on the morning terminator side, similarly to the one observed on the north pole. The centre of the dipole from a thermal point of view, as shown in Fig. 1, is 4° offset with respect to the geometric south pole, although this displacement evidently varies with time. The structure of the dipole at different cloud heights and wavelengths is shown in Supplementary Fig. 1.

Figure 3 shows an image of the deep atmospheric structure of the vortex in two of the spectral ‘window’ regions, at wavelengths near 1.74 and 2.3 μm . Radiative transfer models indicate that the radiation at these wavelengths originates about 10–20 and 20–30 km above the surface, respectively^{8,9}. The spatial contrast structure is produced as this radiation passes through the clouds, and is attenuated by cloud layers with differing optical depths^{10–12}. It was found earlier from Venera 15 infrared spectrometry that sulphuric acid is the main component of the clouds in the north-polar region¹³. From Mie theory calculations, at wavelengths $\lambda < 1.27 \mu\text{m}$ the single scattering albedo of sulphuric acid particles is $\omega_0 > 0.9999$, compared to $\omega_0 = 0.988$ at $\lambda = 2.35 \mu\text{m}$. The relative variation of radiance in the near-infrared spectral windows (as shown in Fig. 3 and Supplementary Fig. 1) is compatible with a sulphuric acid composition of the clouds. The increasing thickness of the clouds does not greatly influence the conservative scattering part of the spectrum ($\lambda < 1.27 \mu\text{m}$), as may be seen in Fig. 3 and Supplementary Fig. 1, panel i. This can be considered as the first indication of the sulphuric acid composition of the clouds in the south polar region.

The polar vortex region is typically very cloudy, even though there are occasionally ‘holes’ where it is possible to probe very deeply at a wavelength of 1.74 μm . The outline of the dipole seen in the thermal

(green circle and green spectrum) and dark (red circle and red spectrum), see Supplementary Fig. 1 for further information. The rising of the continuum radiance on the left side of the spectrum (shorter wavelengths) is due to contamination by scattered light coming from the dayside. The behaviour of the windows corresponds to the variation of the cloud optical depth: the intensity does not change significantly in the window with conservative scattering (for wavelengths lower than 1.27 μm , the absorption optical depth of the cloud deck is less than unity) but changes strongly in the 2.3 μm window. The whole of the dipole is not visible at these wavelengths, because the strong reflected solar light from the higher levels on the dayside does not allow the detection of the deeper levels of the structure beyond the terminator. The three-dimensional view of the vortex seen in these images is not typical, and it may have been enhanced by the relatively high emergence angle of these observations, about 40° in the centre and ranging from 20° to 60° from the top left to the bottom right corner.

region corresponding to the upper cloud layer overlaps with the pattern seen in the near infrared, which is largely modulated by the opacity of the lower and middle cloud layers, but the structure is somewhat different (Fig. 3). The images probing the deep atmosphere show that the vortex may extend as far as the base of the cloud layer at about 50 km height, and perhaps deeper.

VIRTIS observations usually show a strong correlation between the details observed at about 5.0 μm and 3.8 μm , suggesting that the radiance at these wavelengths may depend on the thermal emission from clouds at about the same level. In contrast, simultaneous observations at ultraviolet and infrared wavelengths taken on orbit 29 (19 May 2006; Supplementary Fig. 1) show a strong anticorrelation of the dark ultraviolet cloud features and bright emission regions in the infrared in both the dipole and the spiral arm around it. A possible explanation is that the dark ultraviolet features absorb more solar radiation and are actually warmer than the ultraviolet bright features, but heating by solar radiation is less effective at high latitudes in the polar region. Alternatively, bright regions in the 400 nm images of the high-latitude dayside may also be interpreted as being due to higher clouds located below the thermal inversion layer. Such clouds would have lower temperatures and appear dark in the thermal infrared, and the effective level from which radiation comes in the ultraviolet spectral range would be in this case significantly lower than the previously estimated value around 70 km height^{14–16}.

Small-scale features in the images taken at 1.74 μm and 5.05 μm during orbit 38 were tracked to derive winds at different vertical depths. The wind velocity measured at 1.74 μm (assumed to originate at 45–50 km altitude) decreases from $50 \pm 3 \text{ m s}^{-1}$ at latitude 75°S to 0 m s^{-1} at the pole, implying a meridional wind shear of $(3.2 \pm 0.2) \times 10^{-5} \text{ s}^{-1}$. This matches the rotation rate of the large-scale dipole feature at this wavelength. Small-scale features observed in the dipole at 5.05 μm (altitude about 60 km) move with velocities

that decrease from $35 \pm 5 \text{ m s}^{-1}$ at 75° S to 0 m s^{-1} at the pole, implying a meridional wind shear of $(2.2 \pm 0.3) \times 10^{-5} \text{ s}^{-1}$. Both the upper and lower structures move at the same velocity at latitudes poleward of -80° . The mean vertical wind shear at the dipole external limit at -75° is $(1.5 \pm 0.5) \times 10^{-3} \text{ s}^{-1}$, assuming that the images taken at $1.74 \mu\text{m}$ and $5.05 \mu\text{m}$ are sensing at respective altitudes of 50 km and 60 km. The interesting temporal and structural variability of the dipole will be further analysed over the course of the mission.

Received 8 April; accepted 27 August 2007.

1. Taylor, F. W., McCleese, D. J. & Diner, D. J. Polar clearing in the Venus clouds observed from the Pioneer Venus Orbiter. *Nature* **279**, 613–614 (1979).
2. Elson, L. S. Wave instability in the polar region of Venus. *J. Atmos. Sci.* **39**, 2356–2362 (1982).
3. Taylor, F. W. in *Middle Atmosphere of Venus* (eds Schaeffer, K. & Spankuch, D.) 93–97 (Veröffentlichungen des Forschungsberichts Geo- und Kosmoswissenschaften, Vol. 18, Akademie-Verlag Berlin, 1990).
4. Taylor, F. W. *et al.* Temperature, cloud structure, and dynamics of Venus middle atmosphere by infrared remote-sensing from Pioneer Orbiter. *Science* **205**, 65–67 (1979).
5. Drossart, P. *et al.* Scientific goals for the observation of Venus by VIRTIS on ESA/Venus Express mission. *Planet. Space Sci.* (in the press) (<http://dx.doi.org/10.1016/j.pss.2007.01.003>).
6. Piccioni, G. *et al.* VIRTIS: the Visible and Infrared Thermal Imaging Spectrometer (ESA-SP-1295, ESA Publications Division, Noordwijk, The Netherlands, in the press).
7. Schofield, J. T. & Diner, D. J. Rotation of Venus's polar dipole. *Nature* **305**, 116–119 (1983).
8. Bezar, B. *et al.* The deep atmosphere of Venus revealed by high-resolution nightside spectra. *Nature* **345**, 508–511 (1990).
9. Pollack, J. B. *et al.* Near infrared light from Venus' nightside: A spectroscopic analysis. *Icarus* **103**, 1–42 (1993).
10. Allen, D. A. & Crawford, J. W. Cloud structure on the dark side of Venus. *Nature* **307**, 222–224 (1984).
11. Kamp, L. W., Taylor, F. W. & Calcutt, S. B. Structure of the Venus atmosphere for modelling of night side infrared spectra. *Nature* **336**, 360–362 (1988).
12. Crisp, D. *et al.* The nature of the near-infrared features on the Venus night side. *Science* **246**, 506–509 (1989).
13. Zasova, L. V. *et al.* Structure of the Venus atmosphere. *Planet. Space Sci.* **55**, 1712–1729 (2007).
14. Esposito, L. W. *et al.* in *VENUS II: Geology, Geophysics, Atmosphere and Solar Wind Environment* (eds Bougher, S. W., Hunten, D. M. & Phillips, R. J.) 415–458 (Univ. Arizona Press, Tucson, 1997).
15. Murray, B. C. *et al.* Venus: Atmospheric motion and structure from Mariner 10 pictures. *Science* **183**, 1307–1315 (1974).

16. Suomi, V. E. & Limaye, S. S. Venus — further evidence of vortex circulation. *Science* **201**, 1009–1011 (1978).
17. Grinspoon, D. H. *et al.* Probing Venus's cloud structure with Galileo NIMS. *Planet. Space Sci.* **41**, 515–542 (1993).
18. Carlson, R. W. *et al.* Variations in Venus cloud particle properties — A new view of Venus's cloud morphology as observed by the Galileo Near-Infrared Mapping Spectrometer. *Planet. Space Sci.* **41**, 477–485 (1993).

Supplementary Information is linked to the online version of the paper at www.nature.com/nature.

Acknowledgements We acknowledge the work of the entire Venus Express team, which allowed these data to be obtained. We thank ASI, CNES and the other national space agencies that have supported this research.

Author Contributions G.P. and P.D. coordinated the work as Principal Investigators of VIRTIS. A.S.-L. and R.H. contributed to the dynamics calculation and to Supplementary Fig. 1. F.W.T., C.F.W. and L.Z. contributed to the comparison with earlier data and to the finalization of the paper. D.G. contributed to the temperature retrieval model and calculation, M.M. and A.A. contributed to the thermal structure, and S.L. contributed to the coordination of the dynamics study. All authors contributed equally to the planning of the work and data analysis.

Author Information Reprints and permissions information is available at www.nature.com/reprints. Correspondence and requests for materials should be addressed to G.P. (Giuseppe.piccioni@iasf-roma.inaf.it).

***The VIRTIS-Venus Express Technical Team** Eleonora Ammannito²⁴, Alessandra Barbis²⁵, Rainer Berlin²⁶, Carlo Bettanini²⁷, Angelo Boccaccini²⁴, Guillaume Bonnelo²⁸, Marc Bouye²⁹, Fabrizio Capaccioni³⁰, Alejandro Cardesin Moineo³⁰, Francesco Carraro³¹, Giovanni Cherubini²⁵, Massimo Cosi²⁵, Michele Dami²⁵, Maurizio De Nino³², Davide Del Vento³⁰, Marco Di Giampietro²⁵, Alessandro Donati²⁵, Olivier Dupuis²⁹, Sylvie Espinasse³¹, Anna Fabbri²⁵, Agnes Fave²⁹, Iacopo Fikai Veltroni²⁵, Gianrico Filacchione³⁰, Katia Garceran²⁹, Yamina Ghomchi²⁹, Maurizio Giustini²⁵, Brigitte Gondet²⁸, Yann Hello²⁹, Florence Henry²⁹, Stefan Hofer³³, Gerard Huntzinger²⁹, Juergen Kachlicki²⁶, René Knoll²⁹, Kouach Driss²⁹, Alessandro Mazzoni²⁵, Riccardo Melchiorri²⁹, Giuseppe Mondello²⁵, Francesco Monti³², Christian Neumann³³, Fabrizio Nuccilli²⁴, Jerome Parisot²⁹, Claudio Pasqui²⁵, Stefano Perferi²⁵, Gisbert Peter²⁶, Alain Piacentino²⁹, Carlo Pompei²⁵, Jean-Michel Reess²⁹, Jean-Pierre Rivet²⁹, Antonio Romano²⁵, Natalie Russ²⁶, Massimo Santoni²⁵, Adelmo Scarpelli²⁵, Alain Semery²⁹, Alain Soufflot²⁸, Douchane Stefanovitch²⁹, Enrico Suetta²⁵, Fabio Tarchi²⁵, Nazzareno Tonetti²⁵, Federico Tosi²⁴ & Bernd Ulmer²⁶

Affiliations for participants: ²⁴INAF-IFSI, 00133 Rome, Italy. ²⁵Galileo Avionica, Florence, 50013, Italy. ²⁶DLR, 12489 Berlin, Germany. ²⁷Università di Padova, 35131, Italy. ²⁸IAS Orsay, 91405, France. ²⁹LESIA, Obs. de Paris, 92195 Meudon, France. ³⁰INAF-IFSI, 00133 Rome, Italy. ³¹ASI, Rome, 00198, Italy. ³²Techno System Developments, Naples, 80078, Italy. ³³Kayser Threde, Munich, 81379, Germany.